

Direct imaging of a topological nematic phase in a spin-compensated magnet

Weihang Lu,¹ Camron Farhang,¹ Yuchuan Yao,² Pratap Pal,² Hao Zhang,⁴ Shaofeng Han,¹ Shi-Zeng Lin,³ Chang-Beom Eom,² and Jing Xia^{1,*}

¹ Department of Physics and Astronomy, University of California, Irvine, Irvine, CA 92697, USA

² Department of Materials Science and Engineering, University of Wisconsin-Madison, WI 53706, USA.

³ T-4 & Center for Integrated Nanotechnologies (CINT), Los Alamos National Laboratory, Los Alamos, NM 87545, USA

⁴ Department of Physics and Astronomy, The University of Tennessee, Knoxville, Tennessee 37996, USA

* xia.jing@uci.edu

Abstract

Density waves conventionally describe the periodic modulation of charge or spin, yet the spatial modulation of electronic topology has remained elusive. Here, we report the discovery of a Berry-curvature density wave in the noncollinear antiferromagnet Mn_3NiN with compensated spins. Using high-precision Sagnac Kerr microscopy, we directly image micrometer-scale modulations of the Berry curvature. These topological ripples exhibit orientations unpinned to the crystal lattice, forming a nematic phase that spontaneously breaks rotational symmetry. We attribute this instability to field-induced spatial variations of the spin texture driven by competing magnetic interactions. This discovery unveils a new class of collective order in spin-compensated magnets arising from the geometric phase of the wavefunction itself and offering a tunable degree of freedom for topological spintronics based on antiferromagnets and altermagnets.

Introduction

Density waves (such as charge density wave (CDW)¹, spin density wave (SDW)², pair-density wave³, and exciton density wave⁴) play a central role in understanding quantum materials because they represent collective electronic ordering that emerges from strong interactions between electrons, lattice vibrations, and magnetic degrees of freedom. Just as a CDW modulates the scalar charge distribution $\rho(r)$ and a SDW modulates the vector spin density $S(r)$, a Berry-curvature density wave would fill a critical void in this hierarchy by representing the periodic spatial modulation of the electronic topology itself, specifically, the momentum-space Berry curvature $\Omega(r)$ ^{5,6} projected into real space. When density waves form, they break fundamental symmetries of the system, such as translational¹ and rotational symmetry^{7,8}, leading to new ground states with distinct electronic, optical, and magnetic properties. For example, in strongly correlated superconductors like cuprates and iron-based high temperature superconductors, spin and charge density waves, some induced by a magnetic field⁹, are strongly intertwined^{10,11} with their superconductivity, where Cooper pair amplitude could also vary periodically in space establishing a pair density wave¹². As another example, in the fractional quantum Hall system under a high magnetic field at half-filled Landau levels, electrons self-organize into an anisotropic “stripe” phase¹³ where the charge density modulates in one direction, breaking rotational symmetry and leading to strongly direction-dependent transport. The presence of these density waves often signals competing or intertwined phases¹⁰, such as superconductivity, Mott insulation, or topological order, making them an essential probe of the underlying quantum correlations. By tuning external parameters like pressure, temperature, or doping, transitions can be driven between density-wave states and other exotic phases¹⁴⁻¹⁶, offering a powerful platform for discovering and engineering emergent phenomena in quantum materials.

Berry curvature^{5,6} is a geometric property of electronic wavefunctions that acts like a pseudomagnetic field in momentum space, governing electron dynamics. It gives rise to topological effects such as the anomalous Hall effect¹⁷ and quantized Hall plateaus¹⁸⁻²⁰ via the Chern number. It plays a central role in spin-compensated magnets, such as noncollinear antiferromagnets (AFM)²¹ and altermagnets (AM)^{22,23}. Despite negligible magnetization, large anomalous Hall effects (AHE) are observed in AFM²⁴ and in AM^{25,26} driven purely by Berry curvature, offering promising platforms for ultrafast AFM and AM spintronics with minimal stray fields, field robustness, and fast switching²⁷⁻³⁰. Magneto-optic Kerr effect (MOKE)³¹ and X-ray magnetic circular dichroism (XMCD)²³ have been used to directly image the Berry curvature in AFM Mn_3Sn ³¹ and AM MnTe ²³ respectively. These advances raise the intriguing possibility of observing spatial modulations of the Berry curvature, a Berry-curvature density wave, in spin-compensated magnets. Equally important is understanding how such Berry curvature density wave respond to external perturbations such as magnetic fields, which is crucial for advancing AM and AFM spintronic technologies. It is well known that competing magnetic interactions can stabilize long-

wavelength modulated spin textures, such as spirals or magnetic skyrmions. Because the real-space spin texture is closely linked to the momentum-space Berry curvature, noncollinear antiferromagnets provide a promising materials platform to search for Berry-curvature density waves. To resolve the spatial modulation of the Berry curvature, it is crucial that the optical beam size in MOKE imaging be smaller than the period of the spin texture, yet larger than the atomic lattice constant.

Here using precision MOKE imaging, we discover that magnetic fields induce micron-scale spatial modulations in the otherwise uniform Berry curvature of single crystal epitaxial films of AFM Mn_3NiN ^{32–35}, forming Berry curvature density waves. Mn_3NiN belongs to the family of noncollinear antiferromagnets including Mn_3Sn ²⁴, Mn_3Ge ³⁶, Mn_3Pd ³⁷, and Mn_3NiN ³⁴ that exhibit noncollinear spin textures²¹. In the Γ_{4g} spin texture of Mn_3NiN ³³ (Fig.1a), the Mn moments (blue arrows) form a triangular arrangement within the (111) kagome plane (blue triangle). This spin texture generates a nonzero Berry curvature $\Omega(k)$ in momentum space²¹, which is a geometric property of Bloch electrons and can be represented as a pseudovector $\overline{\Omega}_{n0}$ (red arrow in Fig.1a) oriented perpendicular to the kagome plane. In the presence of a Berry curvature density wave, the uniform pseudovector $\overline{\Omega}_{n0}$ becomes modulated in space, forming a pattern $\overline{\Omega}_n(\vec{r})$ as shown in Fig.1b with wavelength l . Experimentally, Berry curvature manifests in both the anomalous Hall effect (AHE) and the magneto-optical Kerr effect (MOKE) in these materials. The intrinsic anomalous Hall conductivity is given by: $\sigma_{xy} = \frac{-e^2}{2\pi^3\hbar} \int_{\text{BZ}} dk \Omega(k)$ (eq.1), where σ_{xy} is the anomalous Hall conductivity, $\Omega(k) = \sum_n f[\epsilon_n(k) - \mu] \Omega_n(k)$ is the total momentum-resolved Berry curvature over the occupied bands in the Brillouin zone (BZ) (f is the Fermi distribution function; $\epsilon_n(k)$ is the band energy; μ is the chemical potential). The polar MOKE signal $\theta_K(\omega)$ ³⁸ at optical frequency ω : $\theta_K(\omega) = \text{Re} \left[\frac{-\sigma_{xy}(\omega)}{\sigma_{xx}(\omega) \sqrt{1 + i \left(\frac{4\pi}{\omega} \right) \sigma_{xx}(\omega)}} \right]$ (eq.2) provides a spatially resolved probe of the Berry curvature, where $\sigma_{xx}(\omega)$ and $\sigma_{xy}(\omega)$ are the longitudinal and Hall conductivities at optical frequency ω .

Results

The 40 nm thick single crystal epitaxial (001) Mn_3NiN films used in this study were grown on (001)-oriented $(\text{La}_{0.3}\text{Sr}_{0.7})(\text{Al}_{0.65}\text{Ta}_{0.35})\text{O}_3$ (LSAT) substrates via sputtering. Their detailed structural, transport, and magnetic characterizations have been reported elsewhere^{32,39}, with the antiferromagnetic transition Néel temperature $T_N \sim 240$ K. The magnetic (001) neutron diffraction intensity of a similar Mn_3NiN film emerges sharply below T_N , and remains nearly constant down to 2 K, indicating a fully developed temperature-invariant AFM order parameter³². A small net moment $m_{\text{net}} \sim 0.008 \mu_B/\text{Mn}$, due to spin-orbit coupling (SOC), enables magnetic field (B) switching of the chirality of the Γ_{4g} AFM spin

texture through Zeeman coupling. This chirality switching is accompanied with sign reversals of the Berry curvature $\Omega(k)$, net moment m_{net} , AHE signal σ_{xy} , and MOKE signal θ_K ^{21,31,38,39}. MOKE measurements reported here are performed using a zero-loop Sagnac interferometer microscope^{40–43} in the polar geometry (Fig.1e) operating at the 1550 nm telecommunication wavelength. Its superior 10 nrad MOKE precision stems from its unique design that exclusively detects microscopic time-reversal symmetry breaking (TRSB) while rejecting non-TRSB effects such as anisotropy and vibrations. In a recent MOKE study³⁹ at the same 1550 nm wavelength, we have demonstrated a temperature-invariant spontaneous MOKE response in Mn₃NiN solely from the intrinsic Berry curvature contribution, which is in sharp contrast to the strongly temperature-dependent AHE that is dominated by skew scattering. As $\sigma_{xx}(\omega)$ at 1550 nm is largely temperature independent in Mn₃NiN³⁹, $\theta_K(\omega)$ scales with $\sigma_{xy}(\omega)$ (eq.2), which in turn scales with the Berry curvature integral (eq.1), allowing the accurate imaging of Berry curvatures through spatially-resolved MOKE measurement: $\Omega_n \propto \theta_K$.

In sharp contrast to the smooth Hall effect in bulk transport measurement we reported earlier³², the formation of a density wave is clearly visible in the MOKE image of a Mn₃NiN film taken at $T = 2 K$ and $B = 9 T$ (Fig.1c). The horizontal and vertical ripples in the Kerr signal θ_K exhibit amplitudes of 2 to 4 μrad , which is up to 2% of the full 150 μrad Kerr signal. And they disappear completely either when the magnetic field is removed (Fig.2b), or when it is heated above the Néel temperature (Supplementary Fig.6). These ripples correspond to magnetic-field-induced spatial modulations of Ω_n : Berry curvature density waves. It is important to note that this density wave spontaneously breaks both in-plane translational and rotational symmetries, as the applied magnetic field is oriented out of plane. Interestingly, several regions in Fig.1c display coexisting density waves with nearly orthogonal orientations. The intersection angle between these wave patterns varies continuously from 90° to 150°, as evident in the two-dimensional Fourier transform (Fig.1d), where the red and blue rectangles mark vertically and horizontally oriented stripes, respectively. The spread of orientations within the blue region indicates that the stripe directions are not locked to the Mn₃NiN crystal's threefold rotational symmetry separated by 120°, but rather emerge spontaneously, breaking the rotational symmetry of the lattice (nematicity), likely directed by subtle local symmetry-breaking fields.

The magnetic field is identified as the driving force behind the emergence of the observed Berry curvature density wave. Fig.2a-c show MOKE images of the Berry curvature at $T = 2 K$ during a magnetic field sweep: $B = 9 T, 0 T$, and $-9 T$. The coercive field of Mn₃NiN films is known to be massive below 150 K^{32,39}, so $\pm 9 T$ is not enough to reverse the chirality of the Γ_{4g} antiferromagnetic spin texture (Supplementary Fig. 1). However, the applied field does modify the average Berry curvature, shifting the mean Kerr signal θ_K from 138 μrad at zero-field to 158 and 68 μrad at 9 T and $-9 T$ respectively.

Superimposed on this average Berry curvature, clear density wave patterns appear at $B = \pm 9 T$ (Fig.2a, b) but vanish completely $B = 0$ (Fig.2c). Although the density wave patterns at $B = -9 T$ and $+9 T$ broadly mirror each other, significant intrinsic asymmetries are observed, such as the amplitude discrepancy in the upper regions. These deviations (2 to 4 μrad) are two orders of magnitude larger than the 10 $nrad$ precision of the Sagnac interferometer, indicating that the location of the density wave pattern is not entirely determined by static pinning centers. Instead, the specific spatial texture appears to shift when the magnetic field sweeps across zero: $B = -9 T \rightarrow 0 T \rightarrow +9 T$, a behavior consistent with a soft, collective mode that reconfigures spontaneously upon field cycling.

At least two distinct sets of density waves are observed in both Fig.2a ($B = 9 T$) and Fig.2c ($B = -9 T$). In Fig.2a, the upper region is dominated by vertically oriented density waves, while the lower region exhibits horizontally oriented ones, with both patterns coexisting in the middle. To analyze these density waves in detail, the top and bottom regions of Fig.2a are extracted and shown in Fig.2d and Fig.2f, respectively. The corresponding x- and y- line profiles in Fig.2e and Fig.2g reveal nearly identical characteristics: both waves have an amplitude of approximately 2 μrad and a period of 2.7 μm , despite their orthogonal orientations. All MOKE images obtained in this study consistently demonstrate that the amplitude and period of the Berry curvature density waves are highly reproducible, suggesting that they are likely determined by the intrinsic properties of the antiferromagnet and by external parameters such as the applied magnetic field.

Additional MOKE imaging within the antiferromagnetic phase, performed in the same top region of Fig.2a under varying magnetic fields and temperatures, reveals that the amplitude of the Berry curvature density wave scales with the applied magnetic field B_z , while its period remains essentially constant. A phase diagram summarizing these results is shown in Fig.3a, where each solid data point represents the measured density-wave amplitude extracted from a MOKE image taken at the corresponding temperature (T) and field (B) (Supplementary Figs. 2,3,4,5). Representative MOKE images obtained at $T = 150 K$ under magnetic fields of 9, 5, 2, and 0 T are presented in Fig.3b, plotted as deviations ($\theta_K - \theta_{mean}$) from the average Kerr signal θ_{mean} for clarity. The density-wave amplitude increases systematically with magnetic field, yet its wavelength remains nearly unchanged. A similar trend is observed in the sequence recorded at $T = 2 K$ (Fig.3c), confirming the field-scaling and field-independent periodicity of the Berry curvature density wave.

Importantly, while the amplitude of the density wave scales with magnetic field strength, we found its periodicity instead correlates with changes in the electronic structure. As shown in Fig.4a, MOKE imaging of a slightly nitrogen-deficient Mn_3NiN (40 nm) film at $T = 235 K$ and $B = 9 T$ reveals that anti-doping more than doubles the density-wave period, clearly visible in the noise-filtered image in Fig.4b

(raw data presented in [Supplementary Fig. 9](#)). This density wave vanishes when the sample is heated above the Néel temperature $T_N \sim 240$ K ([Supplementary Fig. 6](#)).

Discussion

The observation of coexisting, orthogonally oriented density waves ([Fig. 2a, c](#)), which are notably decoupled from the threefold (120°) rotational symmetry of the Mn_3NiN lattice, serves as a hallmark of spontaneous rotational symmetry breaking. This identifies the phenomenon as a topological nematic state, where the electronic topology self-organizes into a directional texture governed by subtle local symmetry-breaking fields rather than the rigid crystal manifold. Analogous to the nematic stripe phase in fractional quantum Hall systems^{13,7} and electronic nematicity in correlated superconductors^{10,11}, this state marks the emergence of topological nematicity: a regime where the collective modulation of the geometric phase breaks the point-group symmetry of the lattice.

The wavelength of the observed Berry curvature density wave is much larger than the underlying lattice constant, in sharp contrast to the much shorter wavelengths of conventional commensurate or incommensurate charge and spin density waves¹. Unlike conventional density waves, which originate from electronic instabilities driven by the Fermi wave vector and typically manifest on the atomic scale, the Berry-curvature density wave observed here is a mesoscopic phenomenon. Its formation is driven by competing magnetic interactions that modulate the spin texture over micrometer length scales. Consequently, the resulting topological ripples differ fundamentally from standard CDWs or SDWs: they are collective modes of the geometric phase that emerge at wavelengths thousands of times larger than the unit cell. Consistent with its long wavelength, the orientation of the modulation is not pinned to the crystal symmetry. Both features resemble the nematic phase of the two-dimensional electron gas in fractional quantum Hall systems^{13,7}, where the two-dimensional electronic gas is only weakly coupled to the host GaAs lattice. In the noncollinear antiferromagnet Mn_3NiN , although the orientations of the three Mn spins within each unit cell are fixed by the Mn_3NiN lattice, collective ripples of many such spin textures are effectively free from lattice pinning, forming a long-wavelength, freely oriented Berry curvature density wave.

In the following, we present an effective minimalistic model, incorporating the coupling between conduction electrons and localized spins with competing magnetic interactions, to capture the main features of the observed Berry-curvature density wave. At zero magnetic field, the spins in Mn_3NiN form a 120° coplanar noncollinear order ([Fig. 1a](#)) within each triangular unit of the kagome plane^{44,33}. When an out-of-plane magnetic field \mathbf{B}_z is applied, the spins gradually cant toward the field direction, becoming slightly non-coplanar. The conduction electrons mediate a Ruderman-Kittel-Kasuya-Yosida (RKKY)⁴⁵ interaction between localized moments, which is generally competing in nature. It has been shown that such competing

magnetic interactions in the canted phase can lead to a spatial modulation of the canting angle^{46,47}. An example of such an effective spin Hamiltonian producing this modulated canted phase is presented in the [Supplementary Information](#). As illustrated in [Fig.4c](#), the local canting angle is spatially modulated as a function of distance. A minimal Hamiltonian that includes both conduction electrons and localized spins and spin orbital coupling is given in the method section. The coupling between conduction electrons and the spin order in the presence of spin orbit coupling generates a finite Berry curvature even in the pristine uncanted phase. Experimentally, the observed Berry-curvature modulation has a period on the order of 10 μm , which is much longer than the atomic lattice constant. This justifies the usage of the adiabatic approximation in evaluating the Berry curvature, i.e., computing it from the Hamiltonian for each local canting angle. The results, shown in [Fig.4d, e](#), reveal that the canting-angle modulation indeed gives rise to a spatially modulated Berry curvature consistent with experimental observations. The modulation period depends on the RKKY interaction, which is independent of the magnetic field and in turn is controlled by the conduction-electron density.

This theoretical model is consistent with the observed doubling of density wave period in the slightly nitrogen-deficient Mn_3NiN ([Fig.4b](#)), which establishes a direct causal link between the bulk electronic structure and the macroscopic topological texture. Both the canting angle and the amplitude of its modulation increase with field³⁸. Because the spatial modulation in the spin texture is determined by the competing RKKY interaction, which depends on the Fermi surface geometry, this result demonstrates that the Berry-curvature density wave can be deterministically tuned via the chemical potential. This tunability enables engineering control of Berry curvature for spintronic applications.

Based on this model, more complex Berry-curvature patterns can emerge. Superposing multiple helices can generate topological textures such as skyrmions⁴⁸ or merons^{49,47} formed from three helices rotated by 120° . In [Fig.4b](#), two nearly perpendicular Berry-curvature density waves interact to produce a checkerboard-like pattern. The above minimal model is expected to apply broadly to other noncollinear antiferromagnets such as Mn_3Sn ²⁴, Mn_3Ge ³⁶, and Mn_3Pd ³⁷, implying the possible existence of Berry-curvature density waves in these systems. Furthermore, while this study establishes the Berry-curvature density wave in a non-collinear antiferromagnet, the underlying mechanism may broadly apply to the emerging class of spin-compensated topological magnets, including altermagnets. In these systems, large Berry curvatures generated by crystal symmetries could similarly succumb to long-wavelength instabilities, even in the absence of net magnetization. Spintronics devices based on these materials have already been demonstrated, including Mn_3Ge -based spin-triplet supercurrent spin valves and SQUID⁵⁰, and Mn_3Sn -based volatile memory⁵¹. The micron-scale Berry-curvature density waves observed here are therefore highly relevant for antiferromagnetic and altermagnetic spintronics: controlled Berry-curvature ripples

could be exploited as active functional elements, while in other cases they may need to be minimized, for instance through magnetic field shielding.

Methods

Film Growth: Stoichiometric single crystal epitaxial 40 nm Mn_3NiN thin films were grown on (001)-oriented $(\text{La}_{0.3}\text{Sr}_{0.7})(\text{Al}_{0.65}\text{Ta}_{0.35})\text{O}_3$ (LSAT) substrates at 650°C under an Ar/N_2 (78%:22%) mixed atmosphere of 10 mTorr by DC reactive magnetron sputtering using a stoichiometric Mn_3Ni target, which was monitored by in-situ reflection high energy electron diffraction (RHEED).

Sagnac MOKE measurements are performed using a zero-loop fiber-optic Sagnac interferometer⁵² microscope^{42,43}. Upon reflection from the sample the nonreciprocal phase shift $\Delta\varphi$ between the two counterpropagating circularly polarized beams is twice the Kerr rotation $\Delta\varphi = 2\theta_K$. The detailed operation of a Sagnac interferometer is described in the [Supplementary Information](#).

Modulated canting angle and Berry curvature calculations: The modulated canting originates from competing magnetic interactions. The spin texture $\mathbf{S}(\mathbf{r})$ in Mn_3NiN lies mainly in the xy plane and is canted by an external field along z . The local spin energy $\mathcal{H}_s = \int d\mathbf{r}(A S_z^2 - B_z S_z)$ favors uniform canting, while the competing RKKY exchange $\mathcal{H}_{RKKY} = \int d\mathbf{r}d\mathbf{r}'J(\mathbf{r} - \mathbf{r}')S(\mathbf{r})S(\mathbf{r}') = \int d\mathbf{q}J(\mathbf{q})S(\mathbf{q})S(-\mathbf{q})$, with $J(\mathbf{q})$ being minimal at a finite wave vector \mathbf{Q} , drives spatial modulation of spins. Adding an inter-sublattice antiferromagnetic term $\mathcal{H}_{AFM} = J_{AFM} \int d\mathbf{r}(\mathbf{S}_1(\mathbf{r}) \cdot \mathbf{S}_2(\mathbf{r}) + \mathbf{S}_2(\mathbf{r}) \cdot \mathbf{S}_3(\mathbf{r}) + \mathbf{S}_3(\mathbf{r}) \cdot \mathbf{S}_1(\mathbf{r}))$ stabilizes the 120° noncollinear order observed in Mn_3NiN . This modulated canting directly induces a real-space modulation of the local Berry curvature. Periodic variations in the canting angle alter the local electronic band structure, producing a Berry-curvature density wave with the same period as \mathbf{Q} . The modulation wavelength is determined by the RKKY interaction, which depends on the conduction-electron density and Fermi-surface geometry. Details of the calculation is described in the [Supplementary Information](#).

Data availability

Source data are provided with this paper. They have been deposited in a figshare repository with (link TBA).

References:

1. Grüner, G. The dynamics of charge-density waves. *Rev. Mod. Phys.* **60**, 1129–1181 (1988).
2. Overhauser, A. W. Spin Density Waves in an Electron Gas. *Phys. Rev.* **128**, 1437–1452 (1962).
3. Agterberg, D. F. *et al.* The Physics of Pair-Density Waves: Cuprate Superconductors and Beyond. *Annu. Rev. Condens. Matter Phys.* **11**, 231–270 (2020).
4. Zeng, Y. *et al.* Exciton density waves in Coulomb-coupled dual moiré lattices. *Nat. Mater.* **22**, 175–179 (2023).
5. Berry, M. V. Quantal phase factors accompanying adiabatic changes. *Proc. R. Soc. Lond. A* **392**, 45–57 (1984).
6. Vanderbilt, D. *Berry Phases in Electronic Structure Theory*. (Cambridge University Press, Cambridge, 2018).
7. Fradkin, E., Kivelson, S. A., Lawler, M. J., Eisenstein, J. P. & Mackenzie, A. P. Nematic Fermi Fluids in Condensed Matter Physics. *Annual Review of Condensed Matter Physics, Vol 1* **1**, 153–178 (2010).
8. Borzi, R. A. *et al.* Formation of a nematic fluid at high fields in Sr₃Ru₂O₇. *Science* **315**, 214–217 (2007).
9. Wu, T. *et al.* Magnetic-field-induced charge-stripe order in the high-temperature superconductor YBa₂Cu₃O_y. *Nature* **477**, 191–194 (2011).
10. Fradkin, E., Kivelson, S. A. & Tranquada, J. M. Colloquium: Theory of intertwined orders in high temperature superconductors. *Rev. Mod. Phys.* **87**, 457–482 (2015).
11. Chang, J. *et al.* Direct observation of competition between superconductivity and charge density wave order in YBa₂Cu₃O_{6.67}. *Nature Phys* **8**, 871–876 (2012).
12. Liu, Y. *et al.* Pair density wave state in a monolayer high-T_c iron-based superconductor. *Nature* **618**, 934–939 (2023).

13. Lilly, M. P., Cooper, K. B., Eisenstein, J. P., Pfeiffer, L. N. & West, K. W. Evidence for an anisotropic state of two-dimensional electrons in high Landau levels. *Physical Review Letters* **82**, 394–397 (1999).
14. Lilly, M. P., Cooper, K. B., Eisenstein, J. P., Pfeiffer, L. N. & West, K. W. Anisotropic states of two-dimensional electron systems in high Landau levels: Effect of an in-plane magnetic field. *Physical Review Letters* **83**, 824–827 (1999).
15. Xia, J., Eisenstein, J. P., Pfeiffer, L. N. & West, K. W. Evidence for a fractionally quantized Hall state with anisotropic longitudinal transport. *Nature Physics* **7**, 845–848 (2011).
16. Wandel, S. *et al.* Enhanced charge density wave coherence in a light-quenched, high-temperature superconductor. *Science* **376**, 860–864 (2022).
17. Nagaosa, N., Sinova, J., Onoda, S., MacDonald, A. H. & Ong, N. P. Anomalous Hall effect. *Rev. Mod. Phys.* **82**, 1539–1592 (2010).
18. von Klitzing, K., DORDA, G. & Pepper, M. New method for high-accuracy determination of the fine-structure constant based on quantized Hall resistance. *Physical Review Letters* **45**, 494–497 (1980).
19. Tsui, D. C., Stormer, H. L. & Gossard, A. C. Two-dimensional magnetotransport in the extreme quantum limit. *Physical Review Letters* **48**, 1559–1562 (1982).
20. Sprinkart, N., Scheer, E. & Di Bernardo, A. Tutorial: From Topology to Hall Effects—Implications of Berry Phase Physics. *J Low Temp Phys* **217**, 686–719 (2024).
21. Chen, H., Niu, Q. & MacDonald, A. H. Anomalous Hall Effect Arising from Noncollinear Antiferromagnetism. *Phys. Rev. Lett.* **112**, 017205 (2014).
22. Mazin, I. & The PRX Editors. Editorial: Altermagnetism—A New Punch Line of Fundamental Magnetism. *Phys. Rev. X* **12**, 040002 (2022).
23. Amin, O. J. *et al.* Nanoscale imaging and control of altermagnetism in MnTe. *Nature* **636**, 348–353 (2024).

24. Nakatsuji, S., Kiyohara, N. & Higo, T. Large anomalous Hall effect in a non-collinear antiferromagnet at room temperature. *Nature* **527**, 212–215 (2015).
25. Kluczyk, K. P. *et al.* Coexistence of anomalous Hall effect and weak magnetization in a nominally collinear antiferromagnet MnTe. *Phys. Rev. B* **110**, 155201 (2024).
26. Gonzalez Betancourt, R. D. *et al.* Spontaneous Anomalous Hall Effect Arising from an Unconventional Compensated Magnetic Phase in a Semiconductor. *Phys. Rev. Lett.* **130**, 036702 (2023).
27. Jungwirth, T., Marti, X., Wadley, P. & Wunderlich, J. Antiferromagnetic spintronics. *Nature Nanotech* **11**, 231–241 (2016).
28. Baltz, V. *et al.* Antiferromagnetic spintronics. *Rev. Mod. Phys.* **90**, (2018).
29. Šmejkal, L., Mokrousov, Y., Yan, B. & MacDonald, A. H. Topological antiferromagnetic spintronics. *Nature Phys* **14**, 242–251 (2018).
30. He, Q. L., Hughes, T. L., Armitage, N. P., Tokura, Y. & Wang, K. L. Topological spintronics and magnetoelectronics. *Nat. Mater.* **21**, 15–23 (2022).
31. Higo, T. *et al.* Large magneto-optical Kerr effect and imaging of magnetic octupole domains in an antiferromagnetic metal. *Nature Photon* **12**, 73–78 (2018).
32. Yao, Y. *et al.* Direct imaging and control of Berry curvature in noncollinear antiferromagnetic single-crystal thin films. Preprint at <https://doi.org/10.48550/ARXIV.2410.02990> (2024).
33. Gurung, G., Shao, D.-F., Paudel, T. R. & Tsymbal, E. Y. Anomalous Hall conductivity of noncollinear magnetic antiperovskites. *Phys. Rev. Materials* **3**, 044409 (2019).
34. Boldrin, D. *et al.* Anomalous Hall effect in noncollinear antiferromagnetic Mn₃NiN thin films. *Phys. Rev. Mater.* **3**, 094409 (2019).
35. Zhao, K. *et al.* Anomalous Hall effect in the noncollinear antiferromagnetic antiperovskite Mn₃Ni_{1-x}Cu_xN. *Phys. Rev. B* **100**, 045109 (2019).

36. Nayak, A. K. *et al.* Large anomalous Hall effect driven by a nonvanishing Berry curvature in the noncollinear antiferromagnet Mn₃Ge. *Science Advances* **2**, e1501870 (2016).
37. Xu, S. *et al.* Identification of the intrinsic, topological, and extrinsic anomalous Hall effects in noncollinear antiferromagnets. *Newton* **1**, (2025).
38. Feng, W., Guo, G.-Y., Zhou, J., Yao, Y. & Niu, Q. Large magneto-optical Kerr effect in noncollinear antiferromagnets Mn₃X (X = Rh, Ir, Pt). *Phys. Rev. B* **92**, 144426 (2015).
39. Farhang, C. *et al.* Temperature-invariant magneto-optical Kerr effect in a noncollinear antiferromagnet. Preprint at <https://doi.org/10.48550/arxiv.2510.19709> (2025).
40. Xia, J., Maeno, Y., Beyersdorf, P. T., Fejer, M. M. & Kapitulnik, A. High resolution polar Kerr effect measurements of Sr₂RuO₄: Evidence for broken time-reversal symmetry in the superconducting state. *Physical Review Letters* **97**, 167002 (2006).
41. Xia, J. *et al.* Polar Kerr-effect measurements of the high-temperature YBa₂Cu₃O_{6+x} superconductor: Evidence for broken symmetry near the pseudogap temperature. *Physical Review Letters* **100**, 127002 (2008).
42. Gong, C. *et al.* Discovery of intrinsic ferromagnetism in two-dimensional van der Waals crystals. *Nature* **546**, 265–269 (2017).
43. Thomas, S. *et al.* Localized Control of Curie Temperature in Perovskite Oxide Film by Capping-Layer-Induced Octahedral Distortion. *Phys. Rev. Lett.* **119**, 177203 (2017).
44. Wu, M. *et al.* Magnetic structure and lattice contraction in Mn₃NiN. *Journal of Applied Physics* **114**, 123902 (2013).
45. Kittel, C. *Introduction to Solid State Physics*. (Wiley, 2004).
46. Wang, Z., Su, Y., Lin, S.-Z. & Batista, C. D. Skyrmion Crystal from RKKY Interaction Mediated by 2D Electron Gas. *Phys. Rev. Lett.* **124**, 207201 (2020).

47. Wang, Z., Su, Y., Lin, S.-Z. & Batista, C. D. Meron, skyrmion, and vortex crystals in centrosymmetric tetragonal magnets. *Phys. Rev. B* **103**, 104408 (2021).
48. Mühlbauer, S. *et al.* Skyrmion Lattice in a Chiral Magnet. *Science* **323**, 915–919 (2009).
49. Yu, X. Z. *et al.* Transformation between meron and skyrmion topological spin textures in a chiral magnet. *Nature* **564**, 95–98 (2018).
50. Jeon, K.-R. *et al.* Chiral antiferromagnetic Josephson junctions as spin-triplet supercurrent spin valves and d.c. SQUIDs. *Nat. Nanotechnol.* **18**, 747–753 (2023).
51. Goren, N. *et al.* Antiferromagnetic local volatile memory utilizing non-collinear Mn₃Sn thin films and chiral gating. *Commun Mater* **6**, 238 (2025).
52. Xia, J., Beyersdorf, P. T., Fejer, M. M. & Kapitulnik, A. Modified Sagnac interferometer for high-sensitivity magneto-optic measurements at cryogenic temperatures. *Appl Phys Lett* **89**, 062508 (2006).

Acknowledgements

This project was supported by NSF award DMR-2419425 and the Gordon and Betty Moore Foundation EPIQS Initiative, Grant # GBMF10276 awarded to J.X.. C.B.E. acknowledges support for this research through a Vannevar Bush Faculty Fellowship (ONR N00014-20-1-2844) and the Gordon and Betty Moore Foundation's EPIQS Initiative, Grant GBMF9065 awarded to C.B.E.. S.-Z. L. is supported by the U.S. Department of Energy (DOE) National Nuclear Security Administration (NNSA) under Contract No. 89233218CNA000001 through the Laboratory Directed Research and Development (LDRD) Program and was performed, in part, at the Center for Integrated Nanotechnologies, an Office of Science User Facility operated for the DOE Office of Science, under user Proposals No. 2018BU0010 and No. 2018BU0083.

Author Contributions

J.X. conceived and supervised the project. W.L., C.F., S.H., and J.X. carried out the experimental measurements. Y.Y., P.P., and C.B.E. fabricated and characterized the samples. H.Z. and S.-Z. L. performed theoretical calculation. J.X. analyzed the data and drafted the paper with the input from all authors. All authors contributed to the discussion of the manuscript.

Competing interests

The authors declare no competing interest.

Correspondence and requests for materials should be addressed to Jing Xia, Email: xia.jing@uci.edu.

Figures and Captions

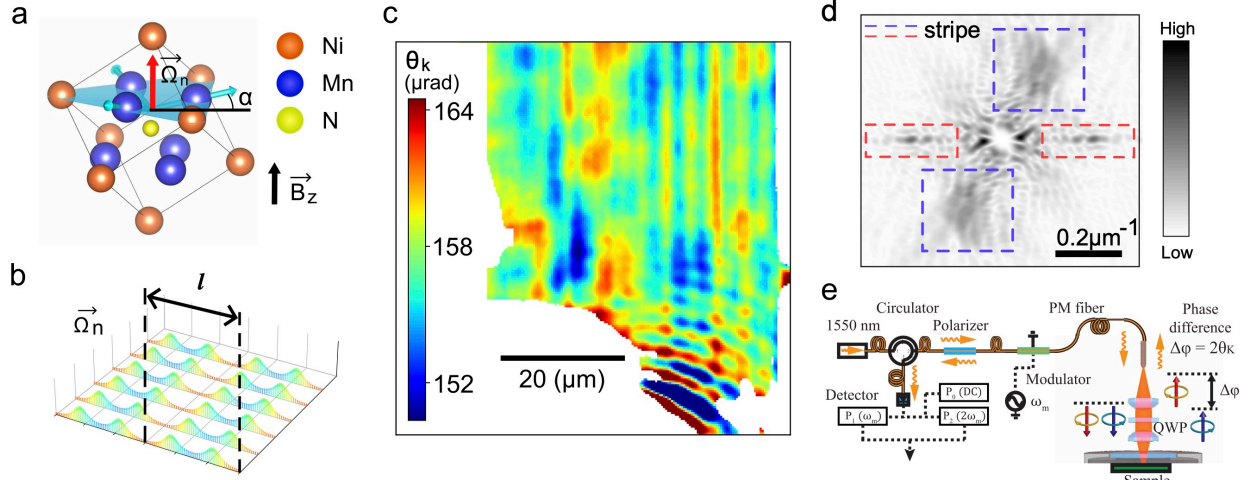


Figure 1. Berry-curvature density wave in noncollinear antiferromagnet Mn_3NiN . **a**, the noncollinear antiferromagnetic (Γ_{4g}) spin texture in Mn_3NiN resulting in a non-zero Berry curvature pseudovector $\overrightarrow{\Omega}_{n0}$ (red arrow). Blue vectors represent Mn spins. **b**, Schematic of a real-space Berry curvature density wave. A “ripple” of the pseudovector $\overrightarrow{\Omega}_n(r)$ emerges in real space with a period l . **c**, MOKE image of the Berry curvature at $T = 2$ K and $B = 9$ T, showing two orthogonally oriented density waves. **d**, Corresponding 2D-FFT with red and blue squares marking the horizontally and vertically oriented density waves respectively. **e**, schematic of the Sagnac interferometer microscope for MOKE imaging.

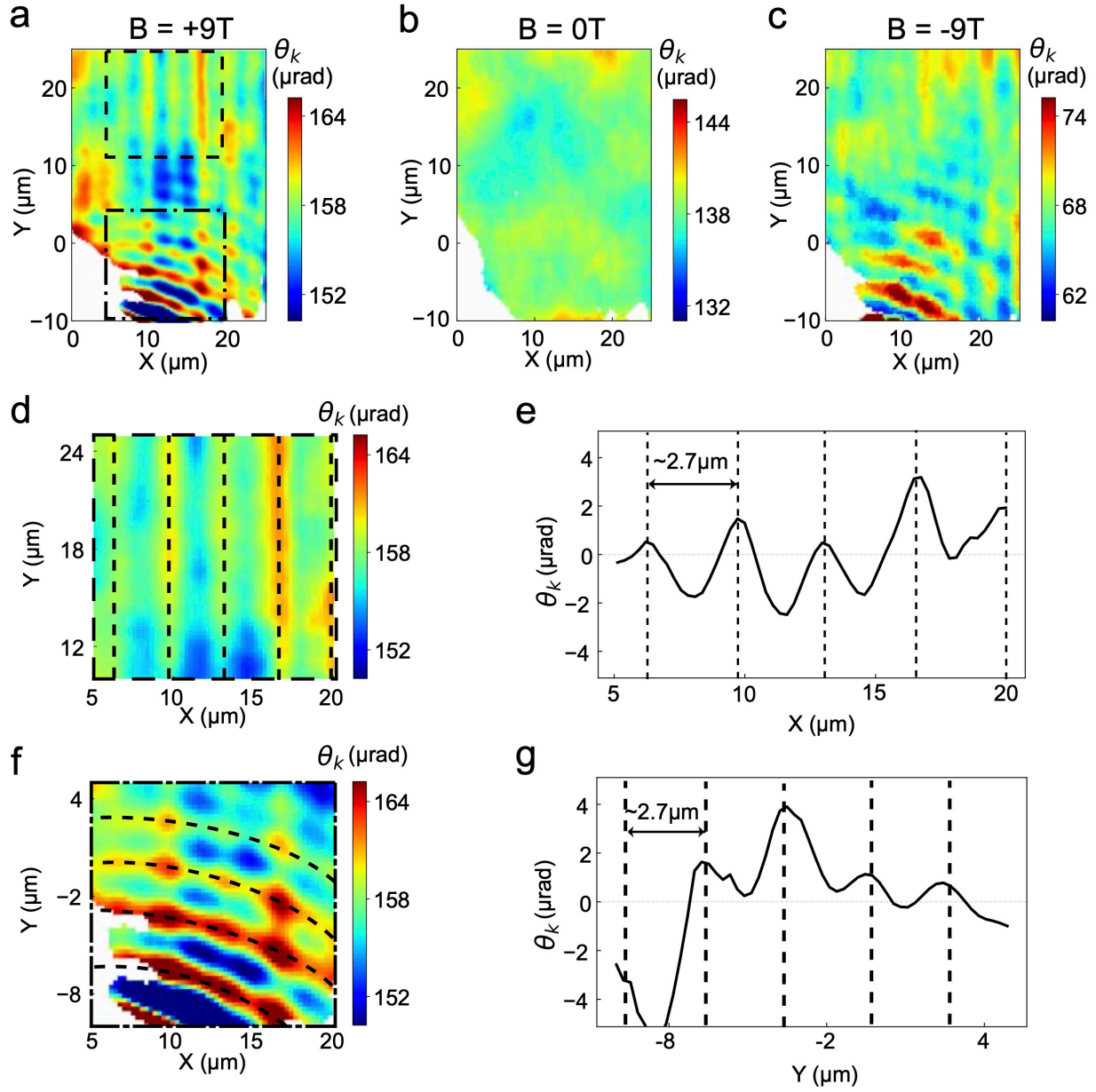


Figure 2. Magnetic field drives Berry-curvature density wave. **a, b, c**, MOKE images of Berry curvature at 2 K, taken with an applied magnetic field of 9 T, 0 T, and -9 T respectively. Note the emergence of density wave at ± 9 T, and its absence at zero field. **d, e**, MOKE image and x-line plot respectively of a region with x-direction Berry-curvature density wave taken at 2 K and 9 T. **f, g**, MOKE image and y-line plot respectively of a region with y-direction Berry-curvature density wave taken at 2 K and 9 T. Note the identical $2.7\mu\text{m}$ period for these two orthogonally oriented density waves.

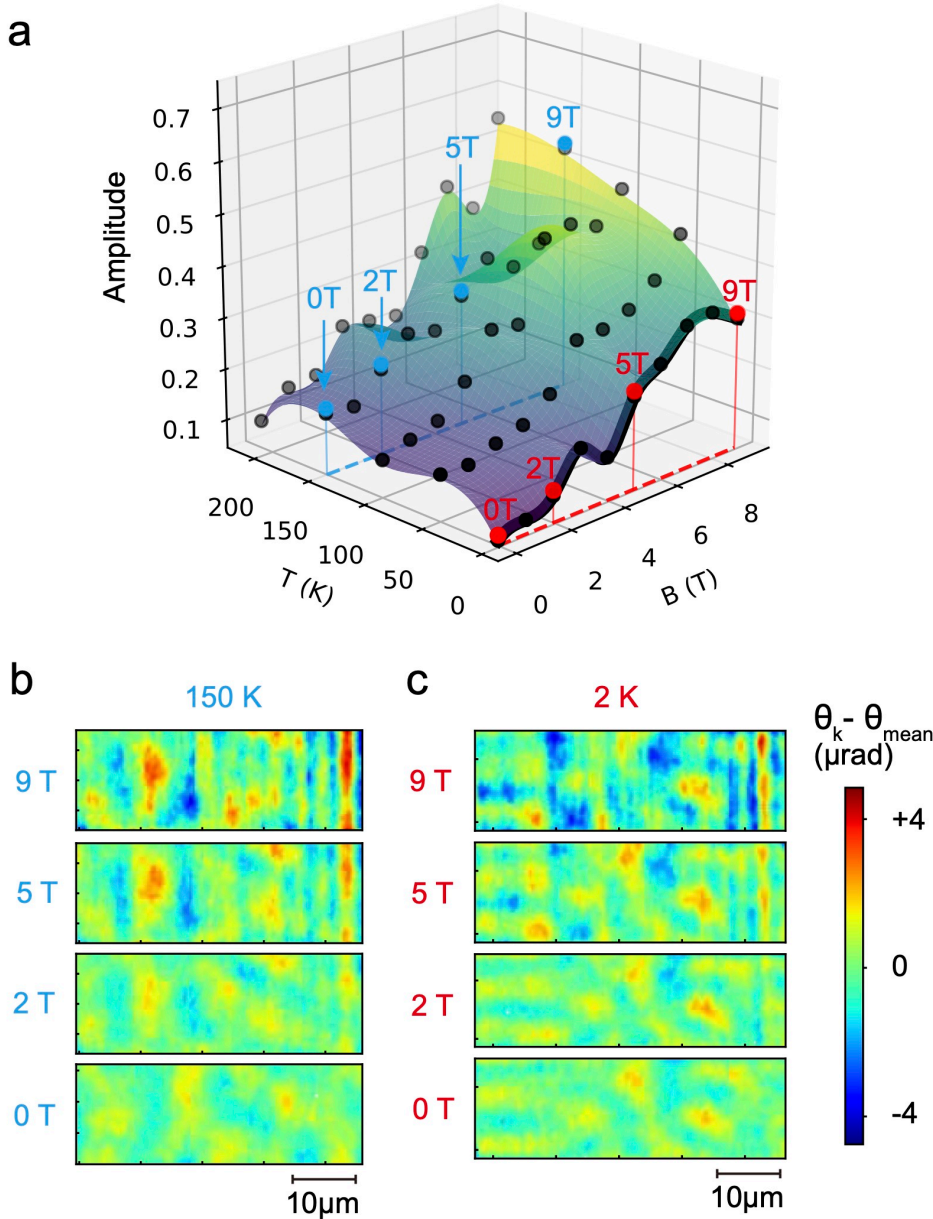


Figure 3. Phase diagram of Berry-curvature density wave. **a**, Amplitude of the Berry-curvature density wave as a function of temperature T and magnetic field B . **b**, **c**, MOKE images of Berry-curvature at representative magnetic fields of 9, 5, 2, and 0 T, taken at 150 K and 2 K respectively. They are plotted as the deviation ($\theta_k - \theta_{mean}$) from the average MOKE signal θ_{mean} for clarity.

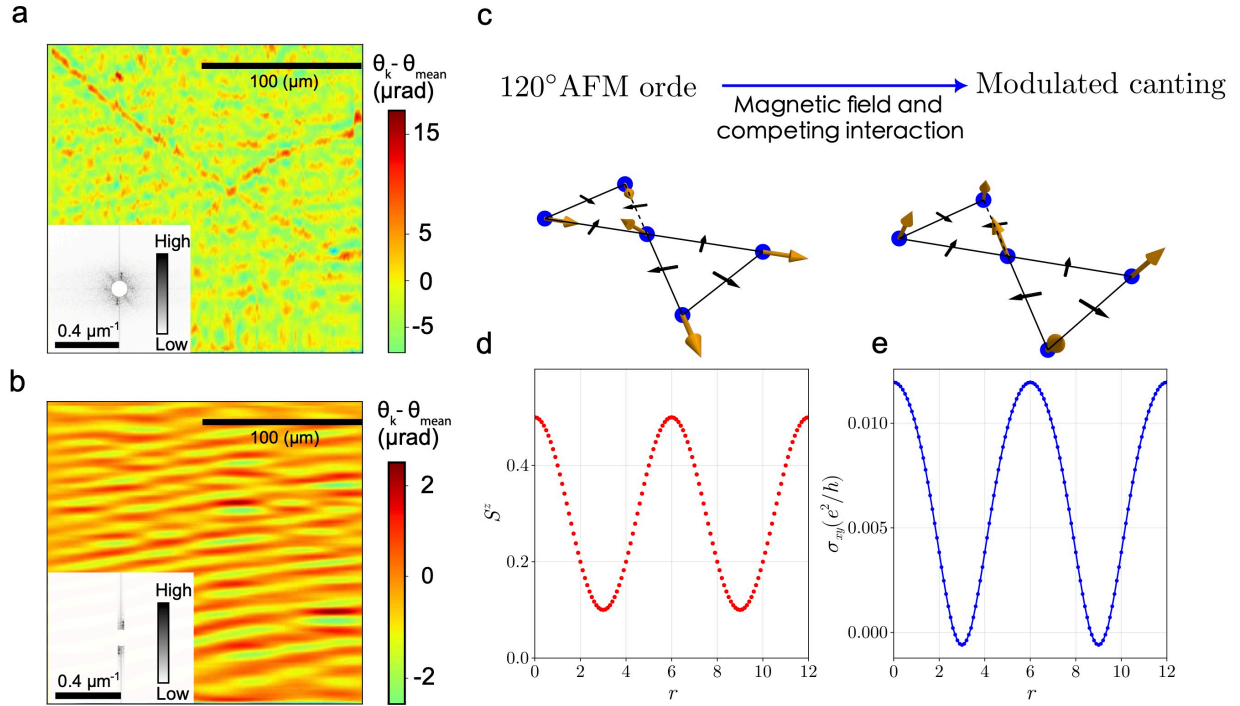


Figure 4. Mechanism of Berry-curvature density wave. **a**, Berry-curvature density wave imaged by MOKE in another Mn_3NiN sample. Insets are Fourier transforms of the image. **b**, noise-filtered MOKE image (raw data presented in [Supplementary Fig. 9](#)), keeping only the horizontally oriented density wave for clarity. **c**, Schematics of the zero-field in-plane 120° magnetic order (left) and the modulated canted antiferromagnetic spin texture (right) induced by an external magnetic field and competing interactions in the Kagome plane. The black arrows indicate the symmetry-allowed spin-orbit vectors $n_{\alpha\beta}$ defined in the [Supplementary Information](#). **d**, **e**, We use the ansatz, $S^z(r) = \alpha_0 + \alpha \cos\left(\frac{2\pi r}{l}\right)$ to describe the modulated canting of spins. The theoretically calculated Hall conductivity σ_{xy} as a function of distance r , showing the formation of a long wavelength density wave. See [Supplementary Information](#) for details of the calculations.